Journal of Alloys and Compounds 949 (2023) 169839

Contents lists available at ScienceDirect

Journal of Alloys and Compounds

journal homepage: www.elsevier.com/locate/jalcom

Preparation and characterization of metastable β-type titanium alloys with favorable properties for orthopedic applications

Zhijun Guo [a,b,1], Yizhou Huang [c,1], Chunchun Sun [b], Zengxing He [d], Yunfeng Li [d], Hua Qiu [e], Delin Yuan [b], Jinyong Zhang [b], Chenglin Chu [a,*], Baolong Shen [a,*]

[a] School of Materials Science and Engineering, Southeast University, Nanjing 2211189, China
[b] School of Materials and Physics, China University of Mining and Technology, Xuzhou 221116, China
[c] Laboratory of Stem Cell and Tissue Engineering, Orthopedic Research Institute, State Key Laboratory of Biotherapy and Cancer Center, West China Hospital, Sichuan University and Collaborative Innovation Center of Biotherapy, Chengdu 610041, China
[d] State Key Laboratory of Oral Diseases, National Clinical Research Center for Oral Diseases, West China Hospital of Stomatology, Sichuan University, Chengdu 610041, China
[e] Key Laboratory of Oral Diseases Research of Anhui Province, Stomatologic Hospital & College, Anhui Medical University, Hefei 230032, China

ARTICLE INFO

Article history:
Received 28 November 2022
Received in revised form 12 March 2023
Accepted 26 March 2023
Available online 27 March 2023

Keywords:
Metastable β-type titanium alloy
Mechanical property
Corrosion resistance
Cytocompatibility
Osteointegration

ABSTRACT

Titanium (Ti)-based alloys with good mechanical properties are highly desirable for bone implants to achieve long-term clinical success. As non-toxic alloying elements, zirconium (Zr) and molybdenum (Mo) have been employed to improve the mechanical properties of Ti-based alloys. In this work, a series of Ti-Zr-Mo alloys, including Ti-18Zr, Ti-13Mo, and Ti-18Zr-13Mo were prepared and compared for potential orthopedic applications for the first time. The phase composition, microstructure, mechanical properties, corrosion resistance, biocompatibility, and osteointegration performance were systemically investigated. It is found that Ti-18Zr displayed an acicular α′ phase, whereas Ti-13Mo and Ti-18Zr-13Mo exhibited a metastable β phase. Compared with commercially pure Ti (CP-Ti), the prepared Ti-Zr-Mo alloys possessed a higher compressive yield strength and a greater microhardness, because of the solid solution and phase precipitation strengthening of Zr and Mo elements. Furthermore, Ti-18Zr-13Mo and Ti-13Mo demonstrated better corrosion resistance than that of CP-Ti, while Ti-18Zr exhibited an inferior result. The cytocompatibility and osteointegration of prepared alloys were similar to those of CP-Ti. Taken together, the Ti-Zr-Mo alloys investigated in this study present a promising alternative to CP-Ti for orthopedic applications, among which the metastable β-type alloy Ti-18Zr-13Mo is most attractive. Moreover, an appropriate Mo content enhances the mechanical and corrosion resistance properties of Ti-based alloys, whereas a high Zr content may pose an adverse influence on the corrosion resistance, which provides valuable insights into the design and further optimizing of new Ti-Zr-Mo alloys for future biomedical applications.

1. Introduction

Titanium (Ti) and its alloys have been widely used as metallic biomaterials in the clinic, such as artificial hip joints, orthopedic prostheses, and dental implants, due to their attractive properties like the light weight, high strength, excellent corrosion resistance, and good biocompatibility [1,2]. Commercially pure Ti (CP-Ti) and Ti-6Al-4 V are most commonly utilized Ti alloys for bone repair, yet both of them have some disadvantages. Due to a relatively low strength, CP-Ti might fracture under complex stress *in vivo*; particularly, a much higher elastic modulus (100–120 GPa) than that of human bone (10–40 GPa) can produce a stress-shielding effect between the CP-Ti implants and the surrounding bone tissue. For Ti-6Al-4 V alloy, the elastic modulus is up to 110 GPa, which is also too high for bone repair. Furthermore, the release of aluminum and vanadium ions *in vivo* can cause neurodegenerative diseases, such as osteomalacia and Alzheimer's disease [3].

As a transition metal, Ti undergoes allotropic transformation at around 883 °C (*i.e.*, the β-transus temperature of Ti). When the temperature is lower than 883 °C, Ti presents a hexagonal α phase. When the temperature is higher than 883 °C, Ti shows a body

* Correspondence to: School of Materials and Engineering, Southeast University, Room A322, No. 2, Daxue Road, 221189 Nanjing, Jiangsu, China.
E-mail addresses: clchu@seu.edu.cn (C. Chu), blshen@seu.edu.cn (B. Shen).
[1] These authors contributed equally to this work as co-first authors.

https://doi.org/10.1016/j.jallcom.2023.169839
0925-8388/

centered cubic structure β phase. Recently, both metastable and stable β-type Ti alloys have attracted considerable attention for biomedical applications owing to their good biocompatibility and favorable mechanical properties, especially a lower elastic modulus than that of α- or α + β-type Ti alloys [4–6].

It is well known that the addition of molybdenum (Mo), a powerful β-phase stabilizer, can reduce the elastic modulus of Ti alloys and improve their corrosion resistance. Zirconium (Zr), another alloying element with a phase transition temperature similar to that of Ti, is considered as a neutral element when added to the solid solution of Ti alloys. With a great solubility in both α- and β-phase of Ti, Zr increases the strength and corrosion resistance of Ti-based alloys. Indeed, in the periodic table, both Zr and Ti elements belong to Group 4 (according to new IUPAC name) and have similar physicochemical and biological properties. They are without any local or systemic toxic effects after implantation *in vivo*, and thus are recognized as non-toxic and non-allergic elements for biomedical applications [7]. Particularly, as a bioactive material, Zr alloy forms a bone-like apatite layer on its surface *in vivo* [8]. Due to their good corrosion resistance and biocompatibility, Ti-Zr alloys have shown encouraging results for dental implants and have been marketed as implant materials [7].

As an essential trace element in humans, Mo is non-toxic at concentrations lower than 8.5 μg/L [9] and contributes to the acid-base balance in human body [10]. In cell cultures, Mo ions showed a negligible toxic effect on human MG-63 osteoblasts while aluminum and vanadium ions at the same concentration obviously inhibited cell proliferation and function [11]. Because of strong corrosion resistance, Mo is commonly used as a major constituent in biomedical implants, such as Ti-7.5Mo [12] and Ti-12Mo-5Ta [13]. With excellent biocompatibility, Ti-Mo alloys are considered as promising materials for medical applications. For instance, Ti-15Mo is commercially available for orthopedic and dental applications in the clinic [14]. Additionally, it has been reported that Ti-xMo (x = 10–13 wt%) alloys demonstrate a shape memory effect, which is ascribed to the decreasing amount of α" and ω phases along with an increasing content of Mo element [15].

Through a combination of biocompatible alloying elements, Ti-Mo-Zr alloys present a potential substitute for traditional Ti alloys [16–22]. Several studies have characterized the properties of some Ti-Mo-Zr alloys, such as the Ti-12Mo-5Zr [23], Ti-15Zr-xMo [24], Ti-20Zr-xMo [2,25], and Ti-30Zr-xMo alloys [26], with emphasis on their microstructure, mechanical properties, corrosion resistance, and biocompatibility for biomedical applications. Correa et al. have analyzed the effect of Mo content on the properties of Ti-15Zr-xMo alloys in terms of their crystalline structure, microstructure, mechanical properties, and cytotoxicity [24]. They found that the elastic modulus of these alloys decreased gradually with increasing Mo content, and that the Ti-15Zr-15Mo alloy showed the lowest elastic modulus (75 GPa). Despite of some progresses in the literature, the elastic modulus of Ti-Zr-Mo alloys reported currently is still much higher than that of bone, hindering the successful applications for long-term implantation. Furthermore, for most studies, the osseointegration of Ti-Zr-Mo alloys remains unknown, and further *in vivo* investigations are needed in the future.

Based on recent alloy design concepts including the Đ-electron method, the Mo equivalence, and the electron/atom ratio approach, we have designed a series of Ti-Zr-Mo alloys with tailored mechanical properties [27–32]. They showed a combination of high strength and large ductility that are favorable in the fields of aerospace, sporting, automotive, and petrochemical industry. Their deformation mechanisms have been studied in our previous research, while whether they are suitable for biomedical applications remain unknown.

Interestingly, when compared with CP-Ti, metastable β-type Ti alloy Ti-18Zr-13Mo has presented distinct low elastic modules, plasticity and tensile strength [31]. Taking this advantage into account, the present paper aims to explore its potential for bone repair. To further understand the influence of Zr or Mo addition on the properties of alloys, CP-Ti, Ti-13Mo and Ti-18Zr were also included in this study. The phase composition, microstructure, mechanical property, electrochemical corrosion, and passivation film of alloys were characterized and compared. Most importantly, to provide a solid basis for their future orthopedic applications, the biological performances of alloys, including their cytocompatibility *in vitro* and the osteointegration performance after implantation *in vivo*, were systematically determined for the first time, which was sought to identify the best combination of properties for bone repair.

2. Materials and methods

2.1. Material preparation

Different alloy ingots including Ti-18Zr, Ti-13Mo and Ti-18Zr-13Mo (wt%) , with a mass of 60 g each, were melted at least for five times in a vacuum induction melting furnace with a vacuum of 5.0×10^{-3} Pa to ensure the homogeneity. The purity of Ti, Mo and Zr materials is ≥ 99.8%. Afterwards, the cast ingots were homogenized at 1173 K for 24 h in a vertical quenching tubular furnace with a heating rate of 10 K/min and a vacuum of $\sim 5.0 \times 10^{-3}$ Pa. After water quenching, the alloy samples were solution-treated (ST) at 1173 K for 30 min under a vacuum of 2.5×10^{-3} Pa, and then quenched again by water cooling. Before the following tests, the alloy samples (square plates, 10 mm × 10 mm × 2 mm) were successively ground with silicon carbide papers (from 320 to 3000 grits), polished with diamond polishing pastes, followed by ultrasonic cleaning and drying.

2.2. Microstructure and composition analysis

After polish with standard metallographic procedures, the specimens were etched with a solution containing H_2O, HNO_3 and HF (15:3:1, vol%) to remove the precipitations and to reveal the grain boundaries. The phase constitution of prepared alloys was characterized by an X-ray diffraction (XRD) machine (Bruker D8 ADVANCE, Germany) with a Cu Kα radiation (λ = 0.1506 nm) and a 2θ scanning of 20–90° operating at 40 kV and 30 mA. An optical microscopy (OM, GX53-OLYMPUS) was used for metallographic observations.

2.3. Mechanical properties

Hardness measurements were performed at a microhardness tester (VH1102, Wilson, USA) with a loading of 50 g and a dwell time of 12 s. In each group, at least 20 indentations were measured to ensure the data reliability. In the compressive mechanical analysis, the specimens were cut into small cubes (5 mm × 5 mm × 10 mm) by a wire electrical discharge machine and were tested on a universal testing machine (Instron 5982, USA) with a constant compression rate of 1×10^{-3} s^{-1} at room temperature. Each sample was measured for at least three times to ensure the validity. The elastic modulus of alloys was calculated from the compressive strain-stress curves.

2.4. Electrochemical measurement

Electrochemical experiments were performed on a workstation (Interface 1010, Gamry, USA) with a conventional three-electrode system. The specimen, platinum electrode, and saturated calomel

electrode (SCE) were served as the working, counter and reference electrode, respectively. The corrosion measurement was conducted in phosphate buffer solution (PBS, pH = 4) at room temperature. All alloys were covered with epoxy to avoid possible crevice attacks; for each sample, the exposed area was 1 cm^2. Before electrochemical tests, all samples were immersed in PBS for 30 min to form a stable passivation film on the surface. The open circuit potential (OCP) was monitored until its value was stable. Electrochemical impedance spectroscopy (EIS) was conducted at 10^{-2} to 10^5 Hz with an AC amplitude of 10 mV. The EIS curves were analyzed by a ZSimpWin software. Potentiodynamic polarization was conducted from − 1–3.5 V (*vs.* SCE) with a scanning rate of 1 $mV{\cdot}s^{-1}$. The Tafel extrapolation method was used for analysis, and the cathodic branch was mainly considered. All electrochemical tests were repeated three times to ensure data consistency.

2.5. X-ray photoelectron spectroscopy analysis

The prepared alloys were immersed in PBS (pH = 4) for 0.5 h to achieve OCP stabilization. Chemical composition of the passivate films was investigated by an X-ray photoelectron spectroscopy (XPS, ESCALAB 250xi, Thermo Fisher, USA) with an Al Kα radiation (1486.6 eV). The instrument was operated at a constant energy mode, with a pass energy of 20 eV and an X-ray spot size of 900 μm. The XPS spectra of elements were analyzed with a Xpspeak 4.1 software.

2.6. Cytocompatibility analysis

Before cell experiments, the alloy samples (10 mm × 10 mm × 1 mm) were polished, cleaned sequentially with acetone, ethanol, and deionized water for 15 min under sonication, and sterilized in an autoclave. All specimens were placed in 24-well plates. MC3T3-E1 cells were seeded on the surface of alloys at a density of 4×10^4 cells/mL and cultured in Dulbecco's modified Eagle's medium supplemented with 10% FBS and 1% penicillin/streptomycin at 37 ℃ with 5% CO_2. Live/Dead staining and Cell Count Kit-8 (CCK-8) assays were performed after culture for 1, 3 and 5 days respectively. In Live/Dead staining, the cells were washed with PBS for three times, stained with a FDA/PI staining kit (BestBio, Shanghai, China) for 5 min at 37 ℃, and then observed at a fluorescence microscope with the excitation wavelength of 518 nm. In CCK-8 assay, 10 μl CCK-8 solution (Dojindo, Japan) was added to each well and incubated for 1.5 h. The optical density (OD) at 450 nm was measured using a microplate reader. CP-Ti was used as the positive control. The experiment was repeated three times to ensure data consistency.

2.7. In vivo studies

Animal experiments were performed in line with the Principles of Laboratory Animal Care formulated by the National Society for Medical Research and were approved by the Animal Research Committee of West China School of Stomatology, Sichuan University. Twenty-eight Sprague-Dawley rats (female, 3-month-old, weighting at 230–280 g) were randomly assigned into four groups, including the CP-Ti group, the Ti-18Zr group, the Ti-13Mo group, and the Ti-18Zr-13Mo group. The alloy samples were cut into cylindrical rods (Φ: 1 mm; length: 10 mm). After ultrasonic irrigation with ethyl alcohol and deionized water, all alloy samples were sterilized in an autoclave before implantation.

Rats were anesthetized by intraperitoneal injection of 3% pentobarbital (30 mg/kg, Sigma, USA). A hole (Φ: 1 mm) was drilled in parallel to the axis of tibia. The implants were inserted into the marrow cavities; then, soft tissues were sutured, and intramuscular antibiotic injection was given. Eight weeks after operation, rat tibias together with the implants were harvested, fixed in 4% paraformaldehyde, and surveyed by a micro-CT scanner system (Scanco Medical μ-CT 50, Switzerland). The scanning system was running at 90 kV, 200 μA, and 500 ms of integration time. The reconstruction voxel size was 10 μm. The region of interest (ROI) was defined as bone around the implant (400 μm below growth plate, with a ring radius of 250 μm from implant surface, and a thickness of 500 μm). After ROI reconstruction, the following parameters were calculated: (1) bone volume ratio percent (BV/TV), (2) trabecular separation (Tb.Sp), (3) trabecular thickness (Tb.Th), and (4) bone-to-implant contact percent (% osseointegration, %OI). The %OI was defined as the ratio of bone-implant contact area to total lateral surface area in the ROI.

Push-out test was performed after micro-CT analysis. Both distal and proximal end of implants were exposed, and the samples were kept in a plastic mold to maintain a vertical position. The maximal push-out force was detected by a universal material testing system (Instron 5982, USA) at a speed of 1 mm/min. For histological observations, the samples were subjected to undecalcified dissection and stained with 1% toluidine blue. The sections approximately 1 mm below the growth plate were observed at a microscope.

2.8. Statistical analysis

All data were expressed as mean ± standard deviation and analyzed by a SPSS 21 software (IBM Corp, Armonk, NY). One-way ANOVA and Student-Newman-Keuls multiple comparison test were applied to compare the difference among groups. Significant difference was defined as $p < 0.05$.

3. Results and discussion

3.1. The elemental composition, phase and microstructure of prepared alloys

As detailed in Table 1, the main elements in prepared alloys were in concentrations close to their stoichiometric values respectively, and the quantity of impurity was negligible.

wt%: weight percentage.

According to the coefficient of β stabilization, the β phase stability of an alloy is defined as:

$$K_\beta = \sum_{i=1}^{n} \frac{c_i}{\beta_{c,i}} \quad (1)$$

where K_β is the β phase stability coefficient of an alloy; c_i is the concentration of β-stabilizing element in the alloy; $\beta_{c,i}$ is the critical concentration of β-stabilizing element. When the K_β of a Ti alloy is at the range of 1–2.5, it is defined as a metastable β-type alloy [23]. In this study, the K_β of Ti-13Mo and Ti-18Zr-13Mo are 1.3 and 1.75 respectively; thus, they are classified as the metastable β-type Ti alloys.

In the XRD results (Fig. 1a),Ti-18Zr showed only peaks of distorted hexagonal α′ phase, which resulted from the infinite solid solution between Ti and Zr atoms [33]. By contrast, only retained β

Table 1
The elemental composition of prepared alloys analyzed by EDS.

Alloy	Ti (wt%)	Mo (wt%)	Zr (wt%)
Ti-18Zr	83.57	-	16.43
Ti-13Mo	87.90	12.10	-
Ti-18Zr-13Mo	69.17	12.55	17.93

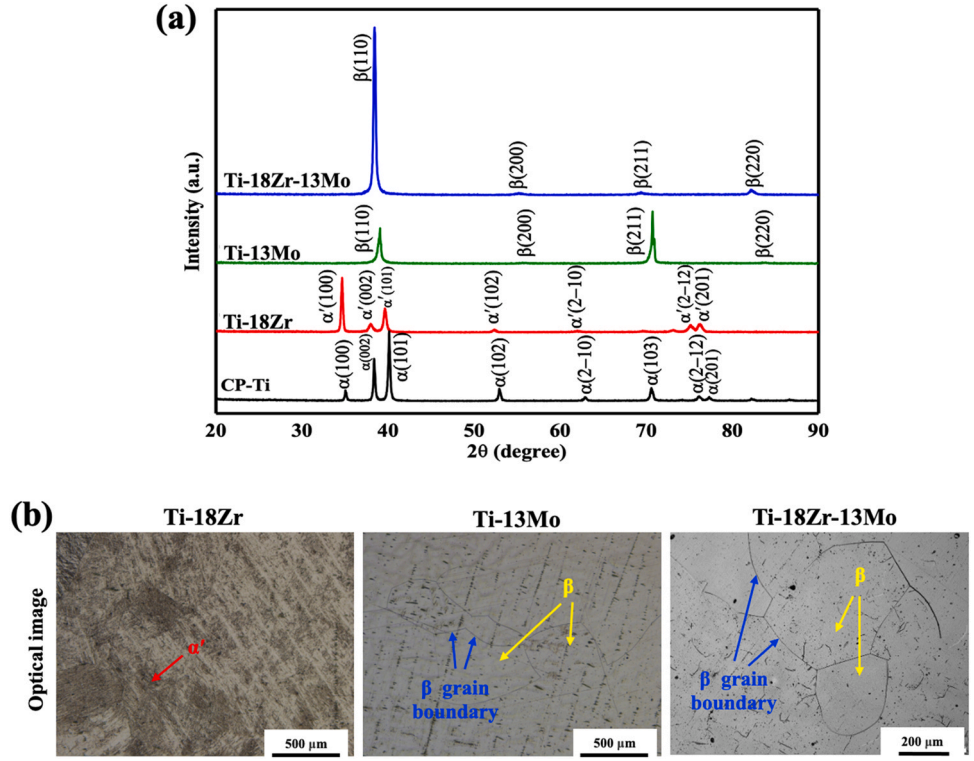

Fig. 1. The phase and microstructure of prepared alloys. (a) XRD pattern of prepared alloys after solution treatment. CP-Ti is served as the control group. (b) Optical microscopy observation of the microstructure of Ti-18Zr, Ti-13Mo and Ti-18Zr-13Mo after solution treatment.

phase with a body-centered cubic structure was observed in Ti-13Mo and Ti-18Zr-13Mo. The microstructure of Ti-13Mo can be ascribed to the existence of Mo element, which acted as a strong stabilizer for β phase; when the content of Mo is higher than 10%, the β phase became the only dominant phase [34]. Additionally, Mo can help to suppress the ω-phase appearance and in many compositions may have a unique property such as a shape memory effect [15,35–37]. Zirconium is considered as a neutral element that does not stabilize α or β phase; however, when Mo exists in the alloy, Zr can act together with the Mo element as a β-phase stabilizing element [2]; consequently, only β phase is observed in Ti-18Zr-13Mo.

When compared with the α phase in CP-Ti and the β phase in Ti-13Mo, those peaks associated with the α′ and β phase of Ti-18Zr and Ti-18Zr-13Mo shifted towards a lower angle respectively. This phenome may be due to the increased lattice constants in these alloys, which are caused by a larger atomic radius of Zr (0.160 nm) than that of Ti (0.147 nm) [38]. Taken together, the XRD results are similar to previous studies [25,33,34,39], revealing that the Ti-18Zr belongs to α-type alloys, while the Ti-13Mo and Ti-18Zr-13Mo are β-type alloys.

Optical analysis was applied to observe the microstructure of alloys. As shown in Fig. 1b, the Ti-18Zr is comprised of typical martensitic α′ phase with an acicular structure, which is similar to previous study [2]. In the Ti-13Mo, irregular coarse β phase grains with a size of about 500 μm were observed, whereas the Ti-18Zr-13Mo presented coarsely equiaxed β crystal grains with a size of 200–500 μm. A large grain size in these alloys is ascribed to the great driving force for grain growth at high temperature [17]. Taken together, these results reveal that when 13% Mo is added to Ti-18Zr, the percentage of acicular α′ phase decreases quickly, while the equiaxed β phase becomes the dominant phase, indicating the β-stabilizing function of Mo element.

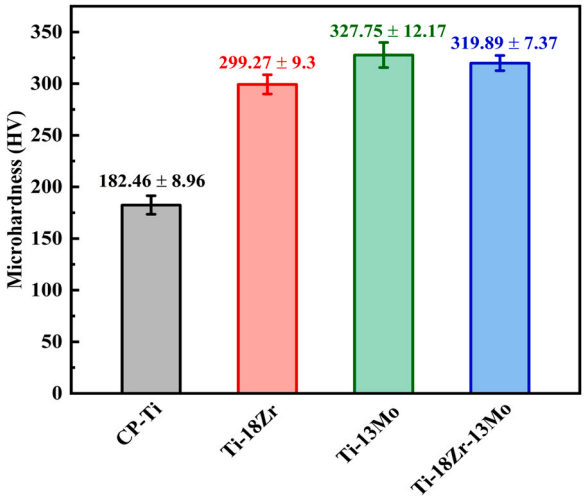

Fig. 2. The microhardness of Ti-18Zr, Ti-13Mo and Ti-18Zr-13Mo after solution treatment. CP-Ti is used as the control group.

3.2. The mechanical properties of prepared alloys

3.2.1. Microhardness

As shown in Fig. 2, all prepared alloys have a higher microhardness (300–330 HV) than that of CP-Ti (~182 HV), which may be due to (1) the solid solution hardening effect and (2) the phase precipitation strengthening effect of Zr and Mo elements [24,40]. Amongst all prepared alloys, Ti-18Zr showed the lowest microhardness (about 300 HV), which can be ascribed to intrinsic

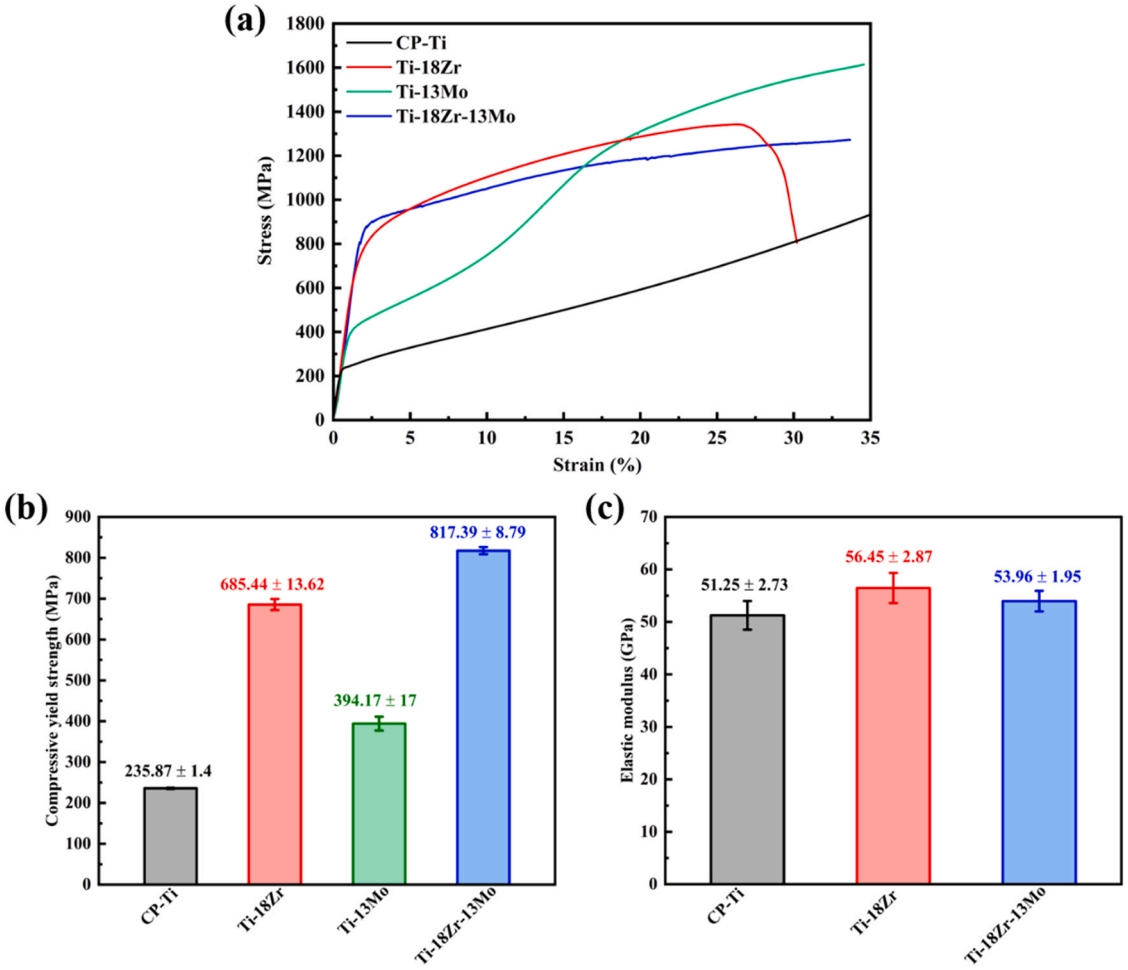

Fig. 3. Compressive mechanical properties of prepared alloys. (a) Compressive stress-strain curves; (b) The compressive yield strength of alloys; (c) The elastic modulus of alloys. CP-Ti is served as the control group.

microstructural contributions, namely, β phase generally had a higher hardness level than that of α′ phase, probably due to a stronger solid solution effects [34]. Although Ti-18Zr has a relatively low microhardness among the prepared alloys, it is still 1.65 times harder than that of CP-Ti, which may result from the lattice distortion and the atomic displacement constraint effects caused by the solid solution strengthening of Zr element [33,41]. Similar results have been reported in Ti-20Zr-xMo alloys [2].

Compared with Ti-18Zr, Ti-13Mo possessed a higher microhardness (Fig. 2), which can be ascribed to a strong solid solution strengthening effect on β phase alloys [34]. Interestingly, although Ti-18Zr-13Mo has both of the solid solution strengthening effects of Mo and Zr element, the microhardness value was a slightly lower than that of Ti-13Mo (Fig. 2), which may be due to an increasement of the β phase. Similarly, it is reported that Ti-20Zr-10Mo possessed a lower hardness than that of Ti-20Zr-7.5Mo, because of an increasement of the β phase, which had the lowest hardness among the phases presented in the Ti-20Zr-xMo system [2]. Since a higher hardness generally indicates a better wear resistance [18], it is obvious that the alloys prepared in this study possess a better wear resistance than that of CP-Ti.

3.2.2. Compressive mechanical properties

Fig. 3a shows the stress-stain curves of prepared alloys, and CP-Ti was served as the control group. It is clearly seen that all prepared alloys exhibited a higher value of compressived yield strength (400–820 MPa) than that of CP-Ti (~236 MPa) (Fig. 3b). Specifically, Ti-13Mo displayed a “double yielding” phenomenon, whereas Ti-18Zr and Ti-18Zr-13Mo did not present any double yielding effect (Fig. 3a). It has been reported that double yielding phenomena originated from shape memory effects. In highly β metastable microstructures, the β phase transforms to a martensite that is stress-assisted in nature [42,43]. As stress loading, the transformation strain from β to martensitic phase is accomadated primarily by internal twinning and partially the rearrangement of martensitic variants induced by stress [42,43]. A minimus in the yield stress (394.17 ± 17 MPa) was observed in Ti-13Mo amongst the prepared alloys, which is supposed that marthensitic transformation occurs during the initial yield [43]. For devices with complex geometry (*e.g.*, the orthopedic nails), hyperelasticity is desirable [44]. In Ti-13Mo and Ti-18Zr-13Mo, no fracture occurred in the compression test, which indicates a good elastoplasticity in these alloys. Due to obvious improvements in the strength, they are expected to avoid fracture after long-term implantation. However, Ti-18Zr showed an lowest elongation to fracture rate of 24.91 ± 0.91%.

As shown in Fig. 3c, the elastic moduli of alloys were evaluated using the stress-strain curves. Due to the double yielding phenomenon, the elastic modulus of Ti-13Mo can not be accurately evaluated through a theoretical way; thus, the corresponding elastic

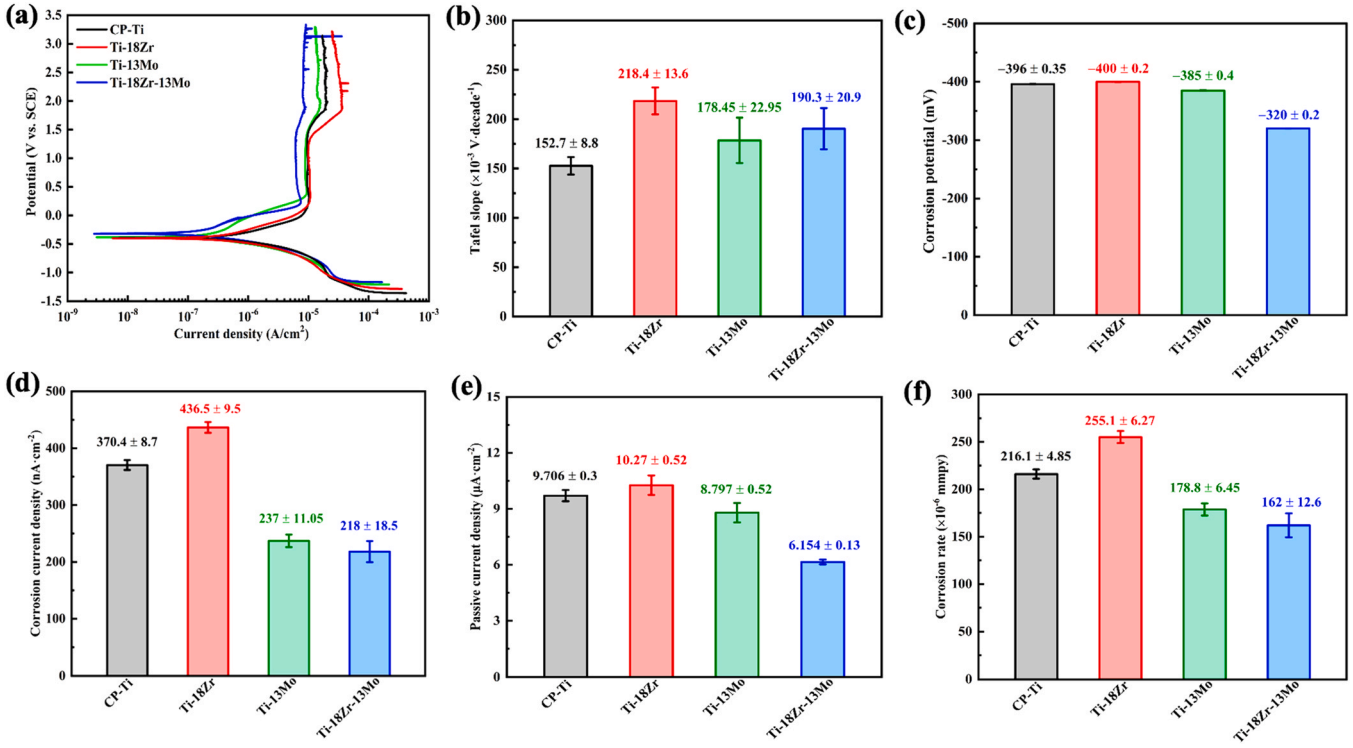

Fig. 4. The potentiodynamic polarization parameters of prepared alloys. (a) Potentiodynamic polarization curves; (b) Tafel slope; (c) Corrosion potential; (d) Corrosion current density; (e) Passive current density; and (f) Corrosion rate of prepared alloys. CP-Ti is served as the control group.

modulus of Ti-13 Mo will not be discussed in this study. Herein, the elastic moduli of Ti-18Zr, Ti-18Zr-13Mo, and CP-Ti with an analogous yielding effect were further investigated for better comparison. According to the compressive stress-strain curves (Fig. 3a), the elastic moduli of Ti-18Zr and Ti-18Zr-13Mo CP-Ti were 56.45 ± 2.87 GPa and 53.96 ± 1.95 GPa respectively (Fig. 3c). At the same condition, the elastic modulus of CP-Ti was 51.25 ± 2.73 GPa (Fig. 3c).

It is known that the elastic modulus of alloys is determined by their atom bonding force and the crystal structure [2,19,23,45]. The higher the atom bonding force, the higher the elastic modulus. Since atomic bonding strength is inversely proportional to the volume of alloy unit cell, the smaller the unit cell volume, the higher the elastic modulus [2]. Because of their large unit cells, the β phase alloys have a lower modulus than that of α or α/β phase alloys [34]. Thus, among the prepared alloys, Ti-18Zr showed the highest elastic modulus, due to the present of α′ phase instead of β phase. Taken together, for orthopedic applications, Ti-18Zr-13Mo showed better mechanical properties than that of CP-Ti.

3.3. Electrochemical characterization of prepared alloys

3.3.1. Potentiodynamic polarization

In view of a slightly acidic microenvironment surrounding the implants at infected or tumor sites *in vivo*, the electrochemical corrosion analysis was carried out in acidic simulated body fluid (*i.e.*, PBS, pH = 4) at room temperature. Fig. 4a illustrates the polarization curves recorded after stabilization. All alloys exhibited a similar polarization behavior: The active solution zone directly entered the stable passivation zone without any activation-passivation transition zone, indicating that all alloys have great passivation ability. The polarization curves exhibited a uniform passivation region, indicating a stable passivation film on the surface. Notably, with a wider passivation region than other groups, the Ti-13Mo and Ti-18Zr-13Mo were more stable in the passivation ability. When the anodic potential was higher than 2 V, sharp increases were observed in the current density. This can be denoted as the start of pit corrosion. Similar corrosion kinetics have been recorded in other studies, such as Ti-50Zr in Ringer solution [46], Ti-6Al-4 V-xZr in NaCl solution [47], and Ti-Zr-Mo-xMn in modified Fusayama artificial saliva solution [48].

The electrochemical corrosion parameters were calculated from the potentiodynamic polarization curves using the Tafel extrapolation method (Fig. 4b-f). As a thermodynamic parameter, the corrosion potential indicates the tendency of corrosion. A lower value implies a more tendency of corrosion. The corrosion potential values in Ti-18Zr-13Mo, Ti-13Mo, CP-Ti and Ti-18Zr were − 320 mV, − 385 mV, − 396 mV, and − 400 mV respectively (Fig. 4c). Therefore, the corrosion tendency was in the order of Ti-18Zr-13Mo < Ti-13Mo < CP -Ti < Ti-18Zr. On the contrary, their corrosion current density values increased gradually (Fig. 4d), and the corrosion rate of Ti-18Zr-13Mo, Ti-13Mo, CP-Ti and Ti-18Zr increased gradually (Fig. 4f).

The passive current density of Ti-18Zr and CP-Ti were higher than those in Ti-18Zr-13Mo and Ti-13Mo (Fig. 4e). Since a lower passive current density value means easier to enter the passivation state, Ti-18Zr-13Mo and Ti-13Mo alloys were easier to achieve a passivation state than Ti-18Zr and CP-Ti. In summary, the corrosion resistance in these alloys is in the order of Ti-18Zr-13Mo > Ti-13Mo > CP-Ti > Ti-

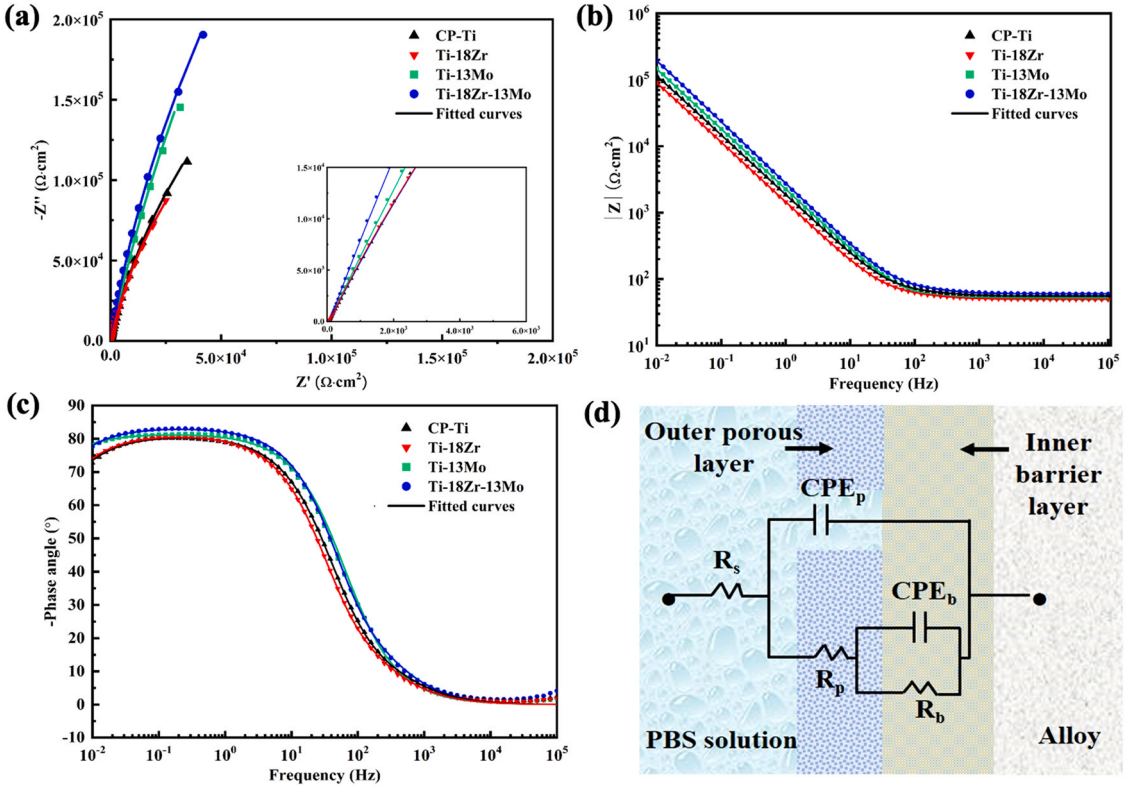

Fig. 5. The electrochemical impedance spectroscopy of prepared alloys. (a) Nyquist plots; (b-c) Bode plots; (b) Impedance magnitude to frequency; (c) Phase angle to frequency; (d) The equivalent circuit model used to fit the impedance spectra of alloys. Rs: the resistance of PBS between the reference and the working electrode; CPEp: the constant phase element (CPE) associated with the outer porous layer; Rp: the charge transfer resistance associated with the outer porous layer; CPEb: the CPE related to the inner compact barrier layer (*i.e.*, the oxide/corrosion product film); Rb: the resistance related to the inner compact barrier layer. CP-Ti is served as the control group.

18Zr. This is consistent with previous studies, which reported that the addition of Mo element improved the corrosion resistance of Ti-Mo alloys [20].

3.3.2. Electrochemical impedance spectroscopy

In the Nyquist plots, all samples showed two capacitive loops (Fig. 5a), which corresponded to different capacitive time constant respectively [49]. The high-frequency capacitive loop is attributed to the double electric layer at the interface between the electrolyte solution and alloys. It shows the charge transfer during the dissolution of metal anode. The low-frequency capacitive loop is related to the corrosion product film of alloys. The exist of arc is attributed to the inhibition of ion diffusion, which is mediated by the corrosion product film [50]. Moreover, the arc radiuses in the Ti-18Zr-13Mo and Ti-13Mo were bigger than the other groups, indicating a higher impedance in these alloys.

The corrosion feature of prepared alloys is demonstrated in the Bode plots (Fig. 5b & c). In the frequency of 10^3-10^5 Hz, the phase and impedance of alloys remained at about 0° and 80 Ω·cm^2 respectively. This indicates that the resistance of electrolyte solution was negligible [48,51]. In the frequency of 10^{-2}-10^3 Hz, the impedance spectrum displayed a linear relation (Fig. 5b), which implies an excellent corrosion resistant of the passivation films [52–54]. At 10^{-2} Hz, the impedance modulus of Ti-18Zr-13Mo, Ti-13Mo, CP-Ti and Ti-18Zr decreased gradually, showing that the corrosion resistance decreased as well [51]. Because of the bi-layered structure of passivation films [48,55,56], a wide plateau was observed at the range of 10^{-2}-10^1 Hz (Fig. 5c). Among the prepared alloys, Ti-18Zr-13Mo showed the highest phase angle. Since a higher phase angle means a better corrosion resistance [51,57,58], Ti-18Zr-13Mo possessed the best corrosion resistance among the samples. Overall, the EIS results showed that the corrosion resistance of Ti-18Zr-13Mo, Ti-13Mo, CP-Ti and Ti-18Zr decreased gradually, which is consistent with the potentiodynamic polarization results.

When Ti and its alloys are immersed in PBS, a passive film containing both an internal dense layer and an external loose layer will form on their surface [59,60]. To obtain the electrochemical parameters, the EIS results were fitted with an equivalent circuit model (Fig. 5d) using a ZsimpWin software [58,61]. Due to the roughness and defects on the sample surface, the current distribution is non-

Table 2
Fitted electrochemical impedance parameters of prepared alloys.

Alloy	R_s (Ω·cm^2)	CPE_p (× 10^{-5} S-sec^n·cm^2)	n_p	R_p (Ω·cm^2)	CPE_b (× 10^{-5} S-sec^n·cm^2)	n_b	R_b (× 10^5 Ω·cm^2)	Chi-Squared/χ^2 (× 10^{-4})
CP-Ti	55.47	5.839	0.9058	35.09	4.446	0.8965	8.483	1.42
Ti-18Zr	49.67	7.756	0.9109	41.39	5.424	0.8957	6.942	1.82
Ti-13Mo	50.83	5.1049	0.91714	44.42	3.2566	0.90638	10.9	5
Ti-18Zr-13Mo	60.02	3.844	0.9342	53.58	2.757	0.9185	20.2	3.406

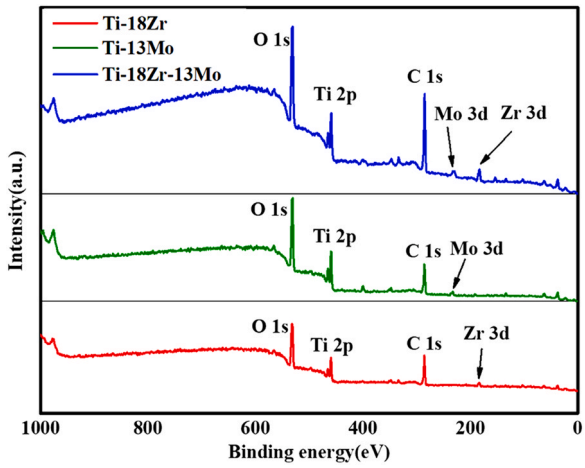

Fig. 6. XPS spectra of the passive film of Ti-18Zr, Ti-13Mo and Ti-18Zr-13Mo respectively.

uniform, and consequently, a constant phase element (CPE) is substituted for pure capacitance [48,50]. The impedance of CPE is defined as following [62]:

$$Z_{CPE} = [Q(j\omega)^n]^{-1} \quad (2)$$

where Q is the capacitance, j and ω ($\omega = 2\pi f$, f: frequency) are the current and the angular frequency respectively, and n is the CPE exponent (ranging from −1 to 1), which is related to the non-uniform distribution of the current because of surface roughness or inhomogeneity.

The fitted results are listed in Table 2. Chi-squared (χ^2) values were in the order of 10^{-4}, suggesting that the fitted results were reliable. The resistance of the inner layer of passivate film (R_b, $6.942\times10^5 \sim 20.2\times10^5\ \Omega\cdot cm^2$) was much higher than that of the outer porous layer (R_p, $35.09 \sim 53.58\ \Omega\cdot cm^2$). This confirms that the corrosion resistance of alloys is closely related to the inner dense layer. The R_b values of Ti-18Zr, CP-Ti, Ti-13Mo and Ti-18Zr-13Mo increased gradually, indicating that the corrosion resistance increased as well. Previous reports have shown that the higher the CPE value, the thinner the passivation film [63,64]. Compared with Ti-18Zr and CP-Ti, a lower CPE_p value was recorded in the Ti-13Mo and Ti-18Zr-13Mo, indicating that their outer layer was thicker.

CPE_b: CPE of the inner compact barrier layer; CPE_p: CPE of the outer porous layer; n_b: CPE exponent of the inner compact barrier layer; n_p: CPE exponent of the outer porous layer; R_b: Resistance of the inner compact barrier layer; R_p: Charge transfer resistance of the outer porous layer; R_s: Resistance of PBS between the reference and working electrode.

3.4. XPS characterization of the passive films

XPS analysis was conducted to investigate the chemical composition of the passive film of alloys. Standard binding energy of C 1 s peak (284.8 eV) was used to calibrate the XPS peaks. As illustrated in Fig. 6, the XPS spectra of Ti-18Zr, Ti-13Mo and Ti-18Zr-13Mo showed characteristic peaks of Ti 2p, Zr 3d, Mo 3d, O 1 s, and C 1 s, revealing that the films contained these elements. The presence of C peak is due to atmospheric contamination. High-resolution scan spectrum of Ti 2p, Zr 3d, Mo 3d and O 1 s peaks are detailed in Fig. 7.

In the Ti-18Zr, the Ti $2p_{1/2}$ and Ti $2p_{3/2}$ peaks were observed at 464.35 eV and 458.64 eV respectively (Fig. 7), which corresponded to Ti^{4+} oxide. The Zr $3d_{3/2}$ and Zr $3d_{5/2}$ peaks were recorded at 184.9 eV and 182.5 eV respectively, which are related to Zr^{4+} oxide. In the O 1 s

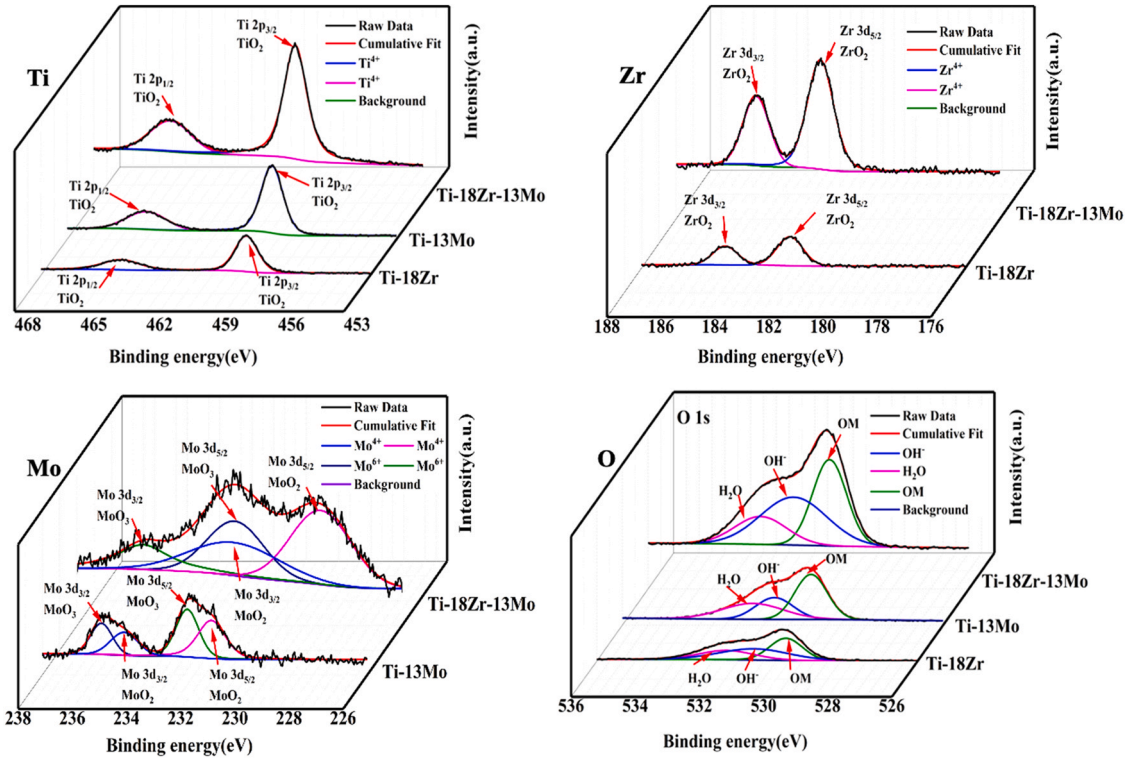

Fig. 7. High-resolution scan spectra of Ti 2p, Zr 3d, Mo 3d and O 1 s peaks in the passive film of prepared alloys. OM: metallic oxide.

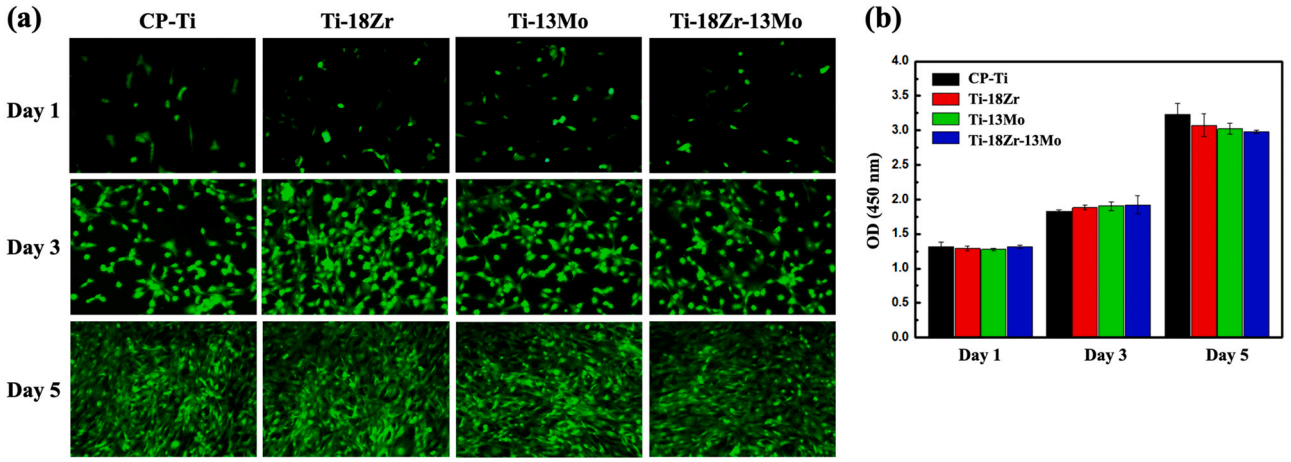

Fig. 8. The cytocompatibility of Ti-18Zr, Ti-13Mo and Ti-18Zr-13Mo. (a) Live/Dead staining of MC3T3-E1 cells cultured on the surface of alloys (200×). Live cells showed green fluorescence, while dead cells exhibited red fluorescence. (b) CCK-8 assay to determine the proliferation of MC3T3-E1 cells cultured on the surface of alloys. CP-Ti was set as the control group.

spectrum, three peaks were recorded, including O^{2-} (530.1 eV), OH^- (531.1 eV) and H_2O (531.96 eV). The H_2O peak was related to the bounded water, the O^{2-} peak was related to TiO_2 and ZrO_2, and the OH^- peak corresponded to the existence of H_2O. These results reveal that the passive film of Ti-18Zr is composed of TiO_2 and ZrO_2. Similarly, it is reported that the surface of Ti-Zr-Cr and Ti-Mo-Zr-xMn contains TiO_2 and ZrO_2 [48,65].

In the Ti-13Mo, the Ti 2p spectrum showed a doublet with Ti $2p_{3/2}$ at 458.67 eV and Ti $2p_{1/2}$ at 464.4 eV (Fig. 7), which were assigned to the Ti-O bond of TiO_2 [20,48]. The Mo 3d spectrum contained two doublets: the peaks at 231.76 eV and 234.98 eV were assigned to the Mo-O bond of MoO_2, whereas the peaks at 232.65 eV and 235.82 eV were assigned to the Mo-O bond of MoO_3 [20,66]. In the O 1 s spectrum, three peaks were observed: (1) the peak at 531.94 eV was indicative of absorbed H_2O; (2) the peak at 531.26 eV was related to OH^-; (3) the peak at 530.12 eV was indicative of O^{2-} [20,66]. Therefore, the passive film is composed of TiO_2, MoO_2 and MoO_3.

In the Ti-18Zr-13Mo, the Ti $2p_{1/2}$ and Ti $2p_{3/2}$ peaks were observed at 464.5 eV and 458.81 eV, whereas Zr $3d_{3/2}$ and Zr $3d_{5/2}$ peaks were observed at 185.03 eV and 182.65 eV respectively (Fig. 7). The Ti 2p peaks were attributed to the Ti-O bond of TiO_2, whereas the Zr 3d peaks were ascribed to the Zr-O bond of ZrO_2. Mo 3d spectrum contained two doublets: the doublet at 229 eV (Mo $3d_{5/2}$) and 232.2 eV (Mo $3d_{3/2}$) corresponded to the Mo-O bond of MoO_2, while the other doublet at 232.16 eV (Mo $3d_{5/2}$) and 235.56 eV (Mo $3d_{3/2}$) was assigned to the Mo-O bond of MoO_3 [66]. The O 1 s spectra consisted of three major peaks: the peak at 532.49 eV was indicative for absorbed H_2O, the peak at 531.46 eV was related to OH^- [20], and the peak at 530.34 eV corresponded with TiO_2, ZrO_2, MoO_2 and MoO_3. Therefore, the passive film is composed of TiO_2, ZrO_2, MoO_2 and MoO_3.

3.5. Cytocompatibility of prepared alloys

Good cytocompatibility is essential for the biomedical applications of alloys. In this study, the cytocompatibility of prepared alloys was determined by the viability and proliferation of MC3T3-E1 cells cultured on the surface of alloys. According to the Live/Dead staining results (Fig. 8a), MC3T3-E1 cells showed a typical fibroblast-like morphology with abundant cell-cell junctions. Good viability (green fluorescence) without obvious cell apoptosis (red fluorescence) was recorded in all groups. A progressive increase in the cell number was noted in all groups over the culture period (Fig. 8a).

Similarly, in the CCK-8 assay result (Fig. 8b), the OD value in each group increased gradually during the cell culture period. No statistically significant difference was noted among the groups at all timepoints ($P > 0.05$). These results strongly suggest that, when compared with CP-Ti, there was a comparable cytocompatibility in the Ti-18Zr, Ti-13Mo and Ti-18Zr-13Mo. It is known that the cytotoxicity of CP-Ti is at the grade of 0–1, indicating that it is non-toxic [7,67]. Based on the above results, it is evident that Ti-18Zr, Ti-13Mo and Ti-18Zr-13Mo possess good cytocompatibility, with a toxicity level close to grade 0–1.

3.6. Osteointegration of prepared alloys

The osteointegration of prepared alloys was determined to explore their application potential for bone repair. As an important factor for long-term clinical success, osteointegration of bone implants is usually defined as a direct structural and functional connection between the implant surface and the surrounding bone tissue [68]. Robust osteointegration is critical for bone-implant stability. To analyze the osteointegration of prepared alloys, the samples were implanted into the drilled cavities in the tibias of rats. Micro-CT analysis, histological staining, and push-out test were carried out to access the peri-implant osteogenesis, the bone-to-implant contact (BIC), and the mechanical stability of alloys.

As shown in the micro-CT images (Fig. 9a), all groups demonstrated abundant bone tissue around the implant. After quantitative analysis, it is found that most of the parameters, including the BV/TV ratio, the Tb.Th value, and the Tb.Sp value were comparable among all groups. However, when compared with CP-Ti, the Ti-18Zr showed a slightly higher BV/TV ratio and a slightly lower Tb.Sp ($p > 0.05$, Fig. 9b). Moreover, the Ti-18Zr and Ti-18Zr-13Mo exhibited a higher %OI value than that of CP-Ti ($p < 0.05$).

Apart from micro-CT analysis, histological evaluation of the osteointegration of alloys was performed using toluidine blue staining. As shown in Fig. 9c, new bone was found in direct contact with the implant surface in each group, indicating that the prepared alloys possess a similar osteoconductivity to that of CP-Ti. According to the result of biomechanical test, the maximum push-out force of implants was comparable among all alloys ($p > 0.05$, Fig. 9d). Based on the above outcomes, it is obvious that the osteointegration of Ti-18Zr, Ti-13Mo and Ti-18Zr-13Mo was comparable to that of CP-Ti, highlighting a good potential for future orthopedic applications.

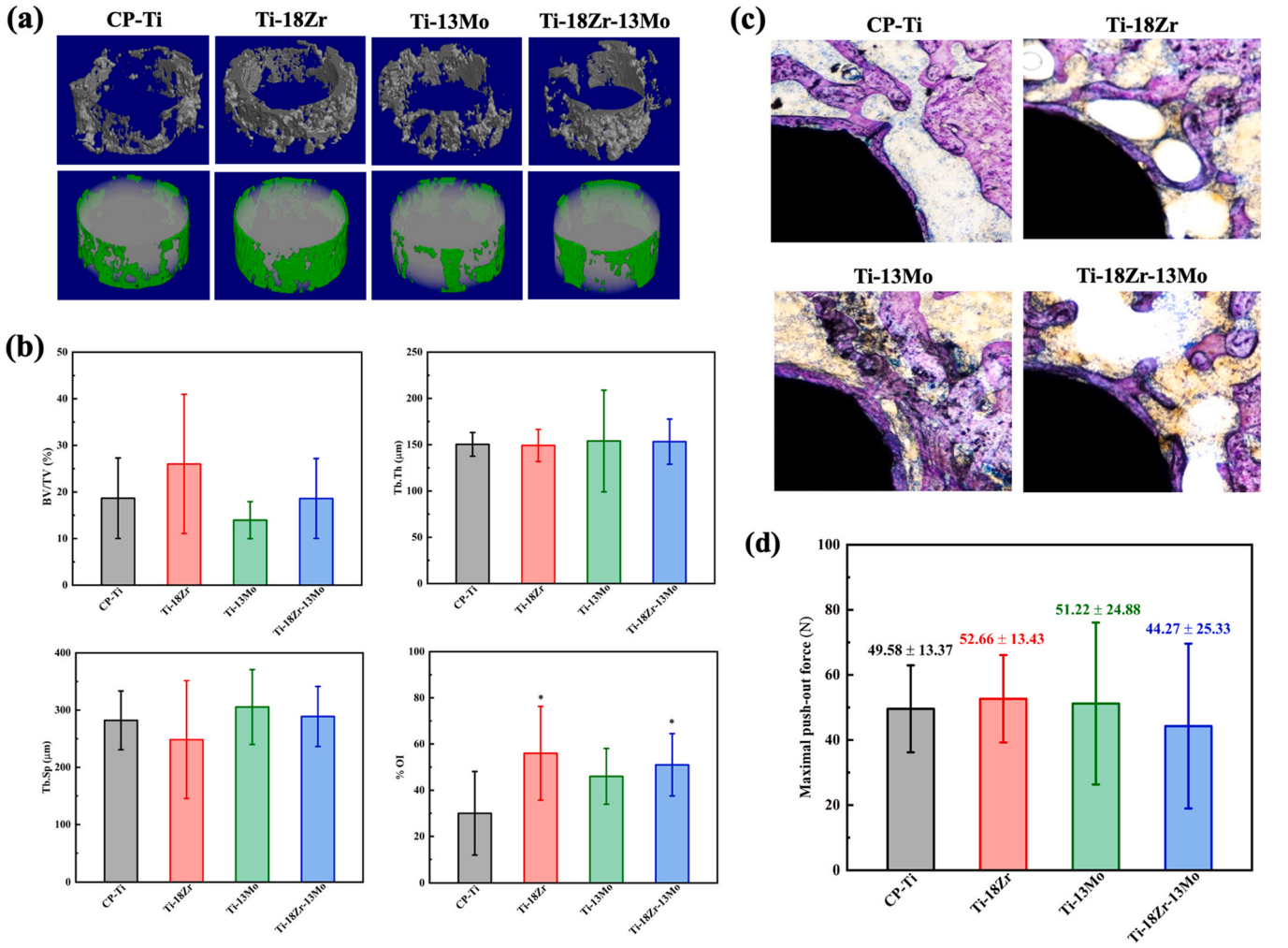

Fig. 9. The osteointegration of prepared alloys after implantation in rat tibia. (a) Micro-CT analysis of new bone formation after implantation. Images on the upper row shows the bone volume around implants, and the down row shows the bone tissue in direct contact with the implants. (b) Quantitative results of the micro-CT evaluation. Parameters are expressed as mean ± SD. BV: bone volume; TV: total volume; Tb.Th: trabecular thickness; Tb.Sp: trabecular separation; OI: osseointegration. * : $p < 0.05$ when compared with CP-Ti. (c) Representative image of toluidine blue staining of peri-implant bone tissue. (d) The maximum push-out force of implants harvested at 8 weeks post-surgery.

4. Conclusions

In summary, a series of Ti-based alloys including Ti-18Zr, Ti-13Mo and Ti-18Zr-13Mo were successfully fabricated with the addition of Zr and/or Mo element. This is the first time the impact of Zr or Mo addition on the properties of Ti-based alloys have been fully investigated in the context of orthopedic applications.The main conclusions are as follows:

1. Depending on the composition of alloying elements, the prepared alloys showed different phases and microstructures. Ti-18Zr consisted of an acicular α′ phase, whereas Ti-13Mo and Ti-18Zr-13Mo showed a metastable β phase.

2. Compared with CP-Ti, the prepared alloys exhibited a greater microhardness and a higher compressive yield strength. Particularly, the compressive yield strength and microhardness of Ti-18Zr-13Mo were ~3.5 times and ~1.75 times higher than those of CP-Ti respectively.

3. In acidic simulated body fluid, all of the prepared alloys formed a passive film on their surface. The corrosion resistance was in the order of Ti-18Zr-13Mo > Ti-13Mo > CP-Ti > Ti-18Zr, indicating that Mo element, instead of Zr element, improved the corrosion resistance.

4. All of the prepared alloys showed excellent cytocompatibility and osteointegration *in vitro* and *in vivo*. The biocompatibility and osteointegration were similar to those of CP-Ti, which is widely applied for bone repair in the clinic.

5. In the context of bone repair, an appropriate Mo content is found to enhance the mechanical and corrosion resistance properties of Ti-based alloys. However, a high Zr content may have an adverse effect on the corrosion resistance. This underlines the importance for further optimizing the alloy system to achieve optimal performance for future practical applications.

6. Among the prepared alloys, metastable β-type alloy Ti-18Zr-13Mo is the most attractive candidate for orthopedic applications, due to the best corrosion resistance, the highest compressive yield strength, and the biocompatibility and osteointegration similar to those of CP-Ti.

CRediT authorship contribution statement

Z.G., Y.H., J.Z., C.C., and B.S.: Conceptualization. **Z.G., Y.H., C.S., Z.H., Y.L., and H.Q.**: Methodology. **Z.G., C.S., Z.H., and H.Q.**: Validation. **Z.G., Y.H., C.S., Z.H., Y.L., H.Q., and D.Y.**: Formal analysis. **Z.G., Y.H., C.S., and D.Y.**: Writing – original draft. **Z.G., Y.H., C.C., and B.S.**: Writing – review & editing. **Z.G., H.Q.**: Funding acquisition. **C.C. and B.S.**: Supervision.

Data availability

Data will be made available on request.

Declaration of Competing Interest

The authors declare that they have no known competing financial interests or personal relationships that could have appeared to influence the work reported in this paper.

Acknowledgements

This work was funded by National Natural Science Foundation of China (52001324), Natural Science Foundation of Jiangsu Province (BK20200643), China Postdoctoral Science Foundation (2020M671641), Fundamental Research Funds for the Central University of Ministry of Education of China (2020QN34), and Research Fund of Anhui Institute of Translational Medicine (2021zhyx-C68).

References

[1] P.F. Ji, B. Li, B.H. Chen, F. Wang, W. Ma, X.Y. Zhang, M.Z. Ma, R.P. Liu, Effect of Nb addition on the stability and biological corrosion resistance of Ti-Zr alloy passivation films, Corros. Sci. 170 (2020) 108696.
[2] P.A.B. Kuroda, M.A.R. Buzalaf, C.R. Grandini, Effect of molybdenum on structure, microstructure and mechanical properties of biomedical Ti-20Zr-Mo alloys, Mater. Sci. Eng. C Mater. Biol. Appl. 67 (2016) 511–515.
[3] S. Nag, R. Banerjee, H.L. Fraser, Microstructural evolution and strengthening mechanisms in Ti–Nb–Zr–Ta, Ti–Mo–Zr–Fe and Ti–15Mo biocompatible alloys, Mater. Sci. Eng. C 25(3) (2005) 357–362.
[4] Z.A.K. Mohsin Talib Mohammed, Arshad N. Siddiquee, Beta titanium alloys: the lowest elastic modulus for biomedical applications: a review, Int. J. Chem. Nucl. Metall. Mater. Eng. 8 (2014) 726–731.
[5] Y. Li, C. Yang, H. Zhao, S. Qu, X. Li, Y. Li, New developments of ti-based alloys for biomedical applications, Materials 7 (3) (2014) 1709–1800.
[6] M.T. Mohammed, Development of a new metastable beta titanium alloy for biomedical applications, Karbala Int. J. Mod. Sci. 3 (4) (2017) 224–230.
[7] P. Ou, C. Hao, J. Liu, R. He, B. Wang, J. Ruan, Cytocompatibility of Ti-xZr alloys as dental implant materials, J. Mater. Sci. Mater. Med. 32 (5) (2021) 50.
[8] L. Nie, Y. Zhan, H. Liu, C. Tang, Novel β-type Zr–Mo–Ti alloys for biological hard tissue replacements, Mater. Des. 53 (2014) 8–12.
[9] Y. Li, C. Wong, J. Xiong, P. Hodgson, C. Wen, Cytotoxicity of titanium and titanium alloying elements, J. Dent. Res. 89 (5) (2010) 493–497.
[10] E.-B. Lee, Mi-Kyung Han, Bong-Jun Kim, Ho-Jun Song, Yeong-Joon Park, Effect of molybdenum on the microstructure, mechanical properties and corrosion behavior of Ti alloys, Int. J. Mater. Res. 105 (9) (2014) 847–853.
[11] N.J. Hallab, C. Vermes, C. Messina, K.A. Roebuck, T.T. Glant, J.J. Jacobs, Concentration- and composition-dependent effects of metal ions on human MG-63 osteoblasts, J. Biomed. Mater. Res. 60 (3) (2002) 420–433.
[12] W.-F. Ho, A comparison of tensile properties and corrosion behavior of cast Ti–7.5Mo with c.p. Ti, Ti–15Mo and Ti–6Al–4V alloys, J. Alloy. Compd. 464 (1–2) (2008) 580–583.
[13] D.M. Gordin, T. Gloriant, G. Texier, I. Thibon, D. Ansel, J.L. Duval, M.D. Nagel, Development of a beta-type Ti-12Mo-5Ta alloy for biomedical applications: cytocompatibility and metallurgical aspects, J. Mater. Sci. Mater. Med. 15 (8) (2004) 885–891.
[14] M. Yan, M. Qian, C. Kong, M.S. Dargusch, Impacts of trace carbon on the microstructure of as-sintered biomedical Ti-15Mo alloy and reassessment of the maximum carbon limit, Acta Biomater. 10 (2) (2014) 1014–1023.
[15] C.H. Wang, M. Liu, P.F. Hu, J.C. Peng, J.A. Wang, Z.M. Ren, G.H. Cao, The effects of α″ and ω phases on the superelasticity and shape memory effect of binary Ti-Mo alloys, J. Alloy. Compd. 720 (2017) 488–496.
[16] D.R. Correa, F.B. Vicente, T.A. Donato, V.E. Arana-Chavez, M.A. Buzalaf, C.R. Grandini, The effect of the solute on the structure, selected mechanical properties, and biocompatibility of Ti-Zr system alloys for dental applications, Mater. Sci. Eng. C Mater. Biol. Appl. 34 (2014) 354–359.
[17] P.F. Ji, B. Li, S.G. Liu, X. Zhang, B.H. Chen, X.Y. Zhang, M.Z. Ma, R.P. Liu, Controlling the corrosion behavior of Ti-Zr alloy by tuning the α/β phase volume fraction and morphology of β phase, J. Alloy. Compd. 825 (2020).
[18] P. Chui, R. Jing, F. Zhang, J. Li, T. Feng, Mechanical properties and corrosion behavior of β-type Ti-Zr-Nb-Mo alloys for biomedical application, J. Alloy. Compd. 842 (2020) 155693.
[19] A.B. Elshalakany, S. Ali, A. Amigó Mata, A.K. Eessaa, P. Mohan, T.A. Osman, V. Amigó Borrás, Microstructure and mechanical properties of Ti-Mo-Zr-Cr biomedical alloys by powder metallurgy, J. Mater. Eng. Perform. 26 (3) (2017) 1262–1271.
[20] J.L. Xu, S.C. Tao, L.Z. Bao, J.M. Luo, Y.F. Zheng, Effects of Mo contents on the microstructure, properties and cytocompatibility of the microwave sintered porous Ti-Mo alloys, Mater. Sci. Eng. C Mater. Biol. Appl. 97 (2019) 156–165.
[21] T. Akimoto, T. Ueno, Y. Tsutsumi, H. Doi, T. Hanawa, N. Wakabayashi, Evaluation of corrosion resistance of implant-use Ti-Zr binary alloys with a range of compositions, J. Biomed. Mater. Res. B Appl. Biomater. 106 (1) (2018) 73–79.
[22] B.-S. Sung, T.-E. Park, Y.-H. Yun, Microstructures and electrochemical behavior of Ti-Mo alloys for biomaterials, Adv. Mater. Sci. Eng. 2015 (2015) 1–7.
[23] C. Zhao, X. Zhang, P. Cao, Mechanical and electrochemical characterization of Ti–12Mo–5Zr alloy for biomedical application, J. Alloy. Compd. 509 (32) (2011) 8235–8238.
[24] D.R.N. Correa, P.A.B. Kuroda, M.L. Lourenco, C.J.C. Fernandes, M.A.R. Buzalaf, W.F. Zambuzzi, C.R. Grandini, Development of Ti-15Zr-Mo alloys for applying as implantable biomedical devices, J. Alloy. Compd. 749 (2018) 163–171.
[25] P.A.B. Kuroda, M.L. Lourenço, D.R.N. Correa, C.R. Grandini, Thermomechanical treatments influence on the phase composition, microstructure, and selected mechanical properties of Ti–20Zr–Mo alloys system for biomedical applications, J. Alloy. Compd. 812 (2020) 152108.
[26] X. Zhao, M. Niinomi, M. Nakai, T. Ishimoto, T. Nakano, Development of high Zr-containing Ti-based alloys with low Young's modulus for use in removable implants, Mater. Sci. Eng. C 31 (7) (2011) 1436–1444.
[27] J.Y. Zhang, J.S. Li, Z. Chen, Q.K. Meng, F. Sun, B.L. Shen, Microstructural evolution of a ductile metastable β titanium alloy with combined TRIP/TWIP effects, J. Alloy. Compd. 699 (2017) 775–782.
[28] J.Y. Zhang, G.F. Chen, Y.Y. Fu, Y. Fan, Z. Chen, J. Xu, H. Chang, Z.H. Zhang, J. Zhou, Z. Sun, B.L. Shen, F. Sun, Strengthening strain-transformable β Ti-alloy via multi-phase nanostructuration, J. Alloy. Compd. 799 (2019) 389–397.
[29] J. Zhang, J. Li, G. Chen, L. Liu, Z. Chen, Q. Meng, B. Shen, F. Sun, F. Prima, Fabrication and characterization of a novel β metastable Ti-Mo-Zr alloy with large ductility and improved yield strength, Mater. Charact. 139 (2018) 421–427.
[30] F. Sun, J.Y. Zhang, M. Marteleur, C. Brozek, E.F. Rauch, M. Veron, P. Vermaut, P.J. Jacques, F. Prima, A new titanium alloy with a combination of high strength, high strain hardening and improved ductility, Scr. Mater. 94 (2015) 17–20.
[31] J. Zhang, F. Sun, Z. Chen, Y. Yang, B. Shen, J. Li, F. Prima, Strong and ductile beta Ti–18Zr–13Mo alloy with multimodal twinning, Mater. Res. Lett. 7 (6) (2019) 251–257.
[32] J. Zhang, B. Qian, Y. Wu, Y. Wang, J. Cheng, Z. Chen, J. Li, F. Sun, F. Prima, A kink-bands reinforced titanium alloy showing 1.3 GPa compressive yield strength: towards extra high-strength/strain-transformable Ti alloys, J. Mater. Sci. Technol. 74 (2021) 21–26.
[33] W.-F. Ho, C.-H. Cheng, C.-H. Pan, S.-C. Wu, H.-C. Hsu, Structure, mechanical properties and grindability of dental Ti–10Zr–X alloys, Mater. Sci. Eng. C 29 (1) (2009) 36–43.
[34] W.F. Ho, C.P. Ju, J.H. Lin, Structure and properties of cast binary Ti-Mo alloys, Biomaterials 20 (22) (1999) 2115–2122.
[35] J.L. Murray, The Mo–Ti (Molybdenum-Titanium) system, Bull. Alloy Phase Diagr. 2 (2) (1981) 185–192.
[36] T. Maeshima, M. Nishida, Shape memory properties of biomedical Ti-Mo-Ag and Ti-Mo-Sn alloys, Mater. Trans. 45 (4) (2004) 1096–1100.
[37] G. He, M. Hagiwara, Ti alloy design strategy for biomedical applications, Mater. Sci. Eng. C 26 (1) (2006) 14–19.
[38] A. Biesiekierski, D. Ping, Y. Li, J. Lin, K.S. Munir, Y. Yamabe-Mitarai, C. Wen, Extraordinary high strength Ti-Zr-Ta alloys through nanoscaled, dual-cubic spinodal reinforcement, Acta Biomater. 53 (2017) 549–558.
[39] P.A.B. Kuroda, M.A.R. Buzalaf, C.R. Grandini, Preparation, microstructural characterization, and selected mechanical properties of Ti-20Zr-2.5Mo and Ti-20Zr-7.5Mo used as biomaterial, Mater. Sci. Forum 869 (2016) 946–951.
[40] W.-F. Ho, S.-C. Wu, S.-K. Hsu, Y.-C. Li, H.-C. Hsu, Effects of molybdenum content on the structure and mechanical properties of as-cast Ti–10Zr-based alloys for biomedical applications, Mater. Sci. Eng. C 32 (3) (2012) 517–522.
[41] H.-C. Hsu, S.-C. Wu, Y.-C. Sung, W.-F. Ho, The structure and mechanical properties of as-cast Zr–Ti alloys, J. Alloy. Compd. 488 (1) (2009) 279–283.
[42] H.Y. Kim, Y. Ohmatsu, J.I. Kim, H. Hosoda, S. Miyazaki, Mechanical properties and shape memory behavior of Ti-Mo-Ga alloys, Mater. Trans. 45 (4) (2004) 1090–1095.
[43] T. Grosdidier, M.J. Philippe, Deformation induced martensite and superelasticity in a beta-metastable titanium alloy, Mater. Sci. Eng. a Struct. 291 (1–2) (2000) 218–223.
[44] J.J. Gao, I. Thibon, D. Laillé, P. Castany, T. Gloriant, Influence of texture and transformation strain on the superelastic performance of a new Ti–20Zr–3Mo–3Sn alloy, Mater. Sci. Eng. A 762 (2019).
[45] M. Geetha, A.K. Singh, R. Asokamani, A.K. Gogia, Ti based biomaterials, the ultimate choice for orthopaedic implants – a review, Prog. Mater. Sci. 54 (3) (2009) 397–425.
[46] N.T. Oliveira, S.R. Biaggio, R.C. Rocha-Filho, N. Bocchi, Electrochemical studies on zirconium and its biocompatible alloys Ti-50Zr at% and Zr-2.5Nb wt% in simulated physiologic media, J. Biomed. Mater. Res. A 74 (3) (2005) 397–407.
[47] C. Xia, Z. Zhang, Z. Feng, B. Pan, X. Zhang, M. Ma, R. Liu, Effect of zirconium content on the microstructure and corrosion behavior of Ti-6Al-4V- x Zr alloys, Corros. Sci. 112 (2016) 687–695.
[48] H. Liu, J. Yang, X. Zhao, Y. Sheng, W. Li, C.-L. Chang, Q. Zhang, Z. Yu, X. Wang, Microstructure, mechanical properties and corrosion behaviors of biomedical Ti-Zr-Mo-xMn alloys for dental application, Corros. Sci. 161 (2019) 108195.
[49] T.T.M. Tran, B. Tribollet, E.M.M. Sutter, New insights into the cathodic dissolution of aluminium using electrochemical methods, Electrochim. Acta 216 (2016) 58–67.
[50] B. Su, L. Luo, B. Wang, Y. Su, L. Wang, R.O. Ritchie, E. Guo, T. Li, H. Yang, H. Huang, J. Guo, H. Fu, Annealed microstructure dependent corrosion behavior of Ti-6Al-3Nb-2Zr-1Mo alloy, J. Mater. Sci. Technol. 62 (2021) 234–248.

[51] B.L. Wang, Y.F. Zheng, L.C. Zhao, Electrochemical corrosion behavior of biomedical Ti-22Nb and Ti-22Nb-6Zr alloys in saline medium, Mater. Corros. 60 (10) (2009) 788–794.
[52] J. Gonzalez, J. Mirza-Rosca, Study of the corrosion behavior of titanium and some of its alloys for biomedical and dental implant applications, J. Electroanal. Chem. (1999) 109–115.
[53] A.K. Shukla, R. Balasubramaniam, S. Bhargava, Properties of passive film formed on CP titanium, Ti–6Al–4V and Ti–13.4Al–29Nb alloys in simulated human body conditions, Intermetallics 13 (6) (2005) 631–637.
[54] A.W.E. Hodgson, Y. Mueller, D. Forster, S. Virtanen, Electrochemical characterisation of passive films on Ti alloys under simulated biological conditions, Electrochim. Acta, 47 (2002) 1913-1923.
[55] N. Dai, L.-C. Zhang, J. Zhang, X. Zhang, Q. Ni, Y. Chen, M. Wu, C. Yang, Distinction in corrosion resistance of selective laser melted Ti-6Al-4V alloy on different planes, Corros. Sci. 111 (2016) 703–710.
[56] D.Q. Martins, W.R. Osório, M.E.P. Souza, R. Caram, A. Garcia, Effects of Zr content on microstructure and corrosion resistance of Ti–30Nb–Zr casting alloys for biomedical applications, Electrochim. Acta 53 (6) (2008) 2809–2817.
[57] W.R. Osorio, P.R. Goulart, G.A. Santos, C.M. Neto, A. Garcia, Effect of dendritic arm spacing on mechanical properties and corrosion resistance of Al 9 wt Pct Si and Zn 27 wt Pct Al alloys, Mater. Trans. (2006) 2525.
[58] W.R. Osório, J.E. Spinelli, I.L. Ferreira, A. Garcia, The roles of macrosegregation and of dendritic array spacings on the electrochemical behavior of an Al–4.5wt% Cu alloy, Electrochim. Acta 52 (9) (2007) 3265–3273.
[59] K. Miura, N. Yamada, S. Hanada, T.K. Jung, E. Itoi, The bone tissue compatibility of a new Ti-Nb-Sn alloy with a low Young's modulus, Acta Biomater. 7 (5) (2011) 2320–2326.
[60] Y.J. Jo, C.M. Lee, H.S. Jang, N.S. Lee, J.H. Suk, W.H. Lee, Mechanical properties of fully porous and porous-surfaced Ti–6Al–4V implants fabricated by electro-discharge-sintering, J. Mater. Process. Technol. 194 (1–3) (2007) 121–125.
[61] S. Tamilselvi, V. Raman, N. Rajendran, Corrosion behaviour of Ti–6Al–7Nb and Ti–6Al–4V ELI alloys in the simulated body fluid solution by electrochemical impedance spectroscopy, Electrochim. Acta 52 (3) (2006) 839–846.
[62] C. Peng, Y. Liu, H. Liu, S. Zhang, C. Bai, Y. Wan, L. Ren, K. Yang, Optimization of annealing treatment and comprehensive properties of Cu-containing Ti6Al4V-xCu alloys, J. Mater. Sci. Technol. 35 (10) (2019) 2121–2131.
[63] J.Re.S. Gudic, M. Klisˇkic, Study of passivation of Al and Al /Sn alloys in borate buffer solutions using electrochemical impedance spectroscopy, Electrochim. Acta (2002) 3009–3016.
[64] A. Robin, O.A.S. Carvalho, S.G. Schneider, S. Schneider, Corrosion behavior of Ti-xNb-13Zr alloys in Ringer's solution, Mater. Corros. 59 (12) (2008) 929–933.
[65] C. Xia, L. Song, S. Liu, B. Chen, T. Yang, D. Liu, Y. Yang, Y. Wang, Q. Li, Influence of Cr addition on microstructure evolution and corrosion behavior of the Ti Zr alloys, Mater. Charact. 174 (2021) 111045.
[66] T. Bhardwaj, M. Shukla, N.K. Prasad, C.P. Paul, K.S. Bindra, Direct laser deposition-additive manufacturing of Ti–15Mo alloy: effect of build orientation induced surface topography on corrosion and bioactivity, Met. Mater. Int. 26 (7) (2019) 1015–1029.
[67] W. Xu, X. Lu, L.N. Wang, Z.M. Shi, S.M. Lv, M. Qian, X.H. Qu, Mechanical properties, in vitro corrosion resistance and biocompatibility of metal injection molded Ti-12Mo alloy for dental applications, J. Mech. Behav. Biomed. Mater. 88 (2018) 534–547.
[68] F. Marco, F. Milena, G. Gianluca, O. Vittoria, Peri-implant osteogenesis in health and osteoporosis, Micron 36 (7–8) (2005) 630–644.